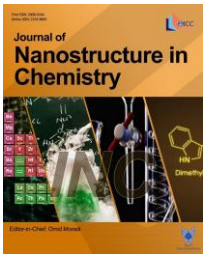

J. Nanostruct Chem. 2026; 16(1): 56-71

Journal of Nanostructure in Chemistry (JNSC)

https://doi.org/10.57647/jnsc.2026.1601.04

Research Article

Gold Nanoisland Microelectrode Micro-Aptamer Sensor with SWASV Readout for EGFR-Positive Lung Cancer Exosomes

Wenxin Yuan[1,2#], Sicong Jiang[1,2#], Chenghong Mao[3], Jiaru Jiang[4], Ke Zhang[5], Dongmei Lin[6], Jianjun Tang[1,2*]

[1] *The First Affiliated Hospital of Nanchang University, Nanchang, Jiangxi, China*

[2] *China-Japan Friendship Jiangxi Hospital, National Regional Center for Respiratory Medicine, Nanchang, Jiangxi, China*

[3] *Department of Clinical Medicine, South Central MinZu University, Wuhan, Hubei, China*

[4] *Department of Pulmonary and Critical Care Medicine, Loudi Central Hospital, Loudi, Hunan, China*

[5] *Department of Pathology, Jiangxi Cancer Hospital & Institute, Jiangxi Clinical Research Center for Cancer, The Second Affiliated Hospital of Nanchang Medical College, Nanchang, Jiangxi, China*

[6] *Department of Intensive Care Unit, Qingpu District Central Hospital, Shanghai, China*

[#] *These authors contributed equally to this work*

[*] **Corresponding authors:** tjj10201@outlook.com

Article History:

Received:
29 October 2025

Revised:
20 November 2025

Accepted:
02 December 2025

Published in Issue:
28 February 2026

Abstract

Non-small cell lung cancer (NSCLC) requires highly sensitive liquid biopsy tools capable of detecting EGFR driven disease and resistance mutations such as T790M, which often evade conventional circulating free DNA assays. Exosomes provide a more reliable biomarker due to their abundance, stability, and enrichment of tumor specific EGFR cargo. Here, we report an ultrasensitive electrochemical microaptasensor specifically designed for the quantitative detection of EGFR positive lung cancer exosomes. The innovation of this work lies in the integration of a thermally dewetted gold nanoisland microelectrode (AuNI ME) which offers a large and Au(111) enriched electroactive surface for high density aptamer immobilization. Additionally, the system utilizes a dual aptamer AND gate recognition strategy using EGFR and CD63 aptamers to ensure exceptional specificity along with a cadmium sulfide quantum dot (CdS QD) amplification system quantified via square wave anodic stripping voltammetry (SWASV). This multi tiered amplification architecture combines nanostructured electrode design, orthogonal dual aptamer recognition, and QD based metal ion amplification to result in a remarkably low limit of detection of 150 particles/mL. This performance outperforms ELISA, NTA, and recent electrochemical exosome assays. The sensor exhibits excellent selectivity, reproducibility, and stability, and demonstrates high recovery ranging from 97.8% to 105.0% in spiked human serum samples. These results highlight the translational potential of this platform as a noninvasive tool for early NSCLC diagnosis and real time therapeutic monitoring.

Keywords: EGFR-positive exosomes; Electrochemical aptasensor; Gold nanoislands; Lung cancer detection; Square wave anodic stripping voltammetry;

Cite this article: Yuan, W., Jiang, S., Mao, Ch., Jiang, J., Zhang, K., Lin, D., Tang, J. Gold Nanoisland Microelectrode Micro-Aptamer Sensor with SWASV Readout for EGFR-Positive Lung Cancer Exosomes. *J Nanostruct Chem* **16**, 56-71 (2026).
https://doi.org/10.57647/jnsc.2026.1601.04

Highlights

This work reports an ultrasensitive gold nanoisland microelectrode aptasensor with dual EGFR and CD63 aptamer recognition and cadmium sulfide quantum dot–square wave anodic stripping voltammetry readout for EGFR-positive lung cancer exosomes. The sensor achieves a limit of detection of 150 particles/mL over a 1.0×10^2–1.0×10^8 particles/mL range, outperforming conventional ELISA and nanoparticle tracking analysis. High specificity toward EGFR-positive vesicles, good fabrication reproducibility, and accurate recovery in spiked serum samples highlight its potential for minimally invasive non-small cell lung cancer monitoring.

1. Introduction

Non-small cell lung cancer (NSCLC) accounts for approximately 85% of all lung malignancies and is a primary cause of cancer-related deaths globally [1]. A significant subset of NSCLC cases is driven by activating mutations in the epidermal growth factor receptor (EGFR) gene, which correlate with sensitivity to targeted therapies using tyrosine kinase inhibitors (TKIs). However, the efficacy of first-generation TKIs is often limited by the development of acquired resistance, with the T790M missense point mutation in exon 20 of the EGFR gene being responsible for approximately 60% of such cases. The detection of the T790M mutation is clinically crucial as it guides the administration of third-generation TKIs like osimertinib, which are highly effective against T790M-positive tumors.

This creates a pressing need for continuous and sensitive monitoring of the patient's mutational status throughout the course of treatment. Traditional tissue biopsies, considered the gold standard for mutation analysis, are invasive procedures associated with significant risks, including bleeding and infection, with complication rates as high as 20%.

Furthermore, their invasive nature makes them unsuitable for the frequent, serial monitoring required to track disease progression and therapeutic resistance. In response to these challenges, liquid biopsy has emerged as a promising non-invasive alternative [2]. Current liquid biopsy approaches predominantly rely on the analysis of circulating free tumor DNA (cfDNA).

However, the clinical utility of cfDNA is hampered by its low sensitivity, particularly in patients with early-stage or localized intrathoracic disease, where the abundance of tumor-derived DNA in the bloodstream is often below the detection limits of current assays like the FDA-approved cobas test, which has a reported sensitivity of only 58% for the T790M mutation. Exosomes, which are nanoscale extracellular vesicles with diameters ranging from 30 to 150 nm, represent a superior class of biomarkers for liquid biopsy. Unlike cfDNA, which is passively released from apoptotic or necrotic cells, exosomes are actively secreted by living cells, including cancer cells, and are found in abundance in various biofluids. Their lipid bilayer membrane protects their molecular cargo—including proteins, lipids, and nucleic acids—from degradation, ensuring stability in circulation [3]. Crucially, exosomes derived from tumor cells are enriched with tumor-specific molecules, such as mutated EGFR protein and its corresponding RNA, providing a concentrated source of biomarkers that can significantly enhance detection sensitivity compared to the fragmented and scarce cfDNA. Studies have demonstrated that analyzing exosomal nucleic acids can achieve sensitivities as high as 92% for detecting the T790M mutation. Despite the diagnostic potential of exosomes, conventional detection methods such as enzyme-linked immunosorbent assay (ELISA) and polymerase chain reaction (PCR) are often limited by complex sample preparation, high costs, and the need for sophisticated laboratory infrastructure, which restricts their application in point-of-care settings [4].

Electrochemical biosensors offer a compelling alternative, providing high sensitivity, rapid response times, portability, and cost-effectiveness [5,6]. To achieve the requisite specificity for exosome detection, aptamers are increasingly favored over traditional antibodies. Aptamers exhibit high affinity and specificity, coupled with superior chemical stability, ease of synthesis and modification, and lower production costs, making them ideal recognition elements for robust biosensor development [7].

This research presents the design and fabrication of a novel, ultrasensitive electrochemical aptasensor for the quantitative detection of EGFR-positive lung cancer exosomes. The sensor platform employs a multi-tiered signal amplification strategy to address the challenge of detecting low-abundance biomarkers. The sensor is built upon a gold nanoisland microelectrode (AuNI-ME), which provides a vastly increased surface area for enhanced electrochemical signaling.

A highly specific, thiolated DNA aptamer targeting the extracellular domain of EGFR is immobilized on the AuNI-ME as the capture probe. A sandwich assay format is completed using a secondary aptamer targeting the ubiquitous exosomal protein CD63, which is conjugated to cadmium sulfide quantum dots (CdS QDs). The binding of target exosomes creates a sandwich complex, and the subsequent acidic dissolution of the captured CdS QDs releases a large number of cadmium ions, which are then quantified using the highly sensitive square wave anodic stripping voltammetry (SWASV) technique.

This synergistic combination of a nanostructured electrode, nanoparticle-based signal amplification, and an

10.57647/jnsc.2026.1601.04

advanced electrochemical readout method is hypothesized to provide a robust and highly sensitive platform for the early diagnosis and monitoring of NSCLC.

2. Materials and Methods

2.1. Reagents and Apparatus

Gold(III) chloride trihydrate, sulfuric acid, 6-mercapto-1-hexanol (MCH), cadmium chloride, sodium sulfide nonahydrate, mercaptoacetic acid (MAA), N-(3-dimethylaminopropyl)-N′-ethylcarbodiimide hydrochloride (EDC), N-hydroxy succinimide (NHS), and nitric acid were purchased from Sinopharm Chemical Reagent Co., Ltd. (Shanghai, China). Phosphate-buffered saline (PBS, pH 7.4), 2-(N-morpholino) ethanesulfonic acid (MES) buffer (pH 6.0), and acetate buffer (0.1 M, pH 4.5) were prepared in-house using analytical-grade reagents and deionized water (18.2 MΩ·cm). Human lung adenocarcinoma cell line (A549, ATCC CCL-185), human lung squamous cell carcinoma cell line (NCI-H520, ATCC HTB-182), and human bronchial epithelial cell line (BEAS-2B, ATCC CRL-9609) were obtained from Cell Bank of the Chinese Academy of Sciences (Shanghai, China). A549 and BEAS-2B cells were cultured in F-12K medium, while NCI-H520 cells were cultured in RPMI-1640 medium. Fetal bovine serum (FBS), exosome-depleted FBS, and penicillin-streptomycin were purchased from Gibco China. Primary antibodies for Western blot analysis (anti-CD9, anti-CD63, anti-CD81, anti-EGFR, and anti-Calnexin) were obtained from Abcam China (Shanghai, China). All DNA aptamers were custom synthesized by Sangon Biotech Co., Ltd. (Shanghai, China), and their sequences are listed in Table 1.

2.2. Cell Culture and Exosome Isolation

A549 cells (EGFR-positive) and BEAS-2B cells (normal control) were cultured in F-12K Medium, while NCI-H520 cells (EGFR-negative lung cancer control) were cultured in RPMI-1640. All media were supplemented with 10% exosome-depleted FBS and 1% penicillin-streptomycin. Cells were maintained in a humidified incubator at 37°C with 5%. For exosome isolation, cells were grown to approximately 80% confluency, after which the conditioned medium was collected. Exosomes were isolated using a differential ultracentrifugation protocol [8]. Briefly, the collected medium was centrifuged sequentially at 300 x g for 10 minutes to remove cells, 2,000 x g for 10 minutes to remove dead cells, and 10,000 x g for 30 minutes at 4°C to remove larger cellular debris and vesicles. The resulting supernatant was filtered through a 0.22 μm filter and then ultracentrifuged at 120,000 x g for 90 minutes at 4°C. The exosome pellet was washed with sterile PBS and subjected to a second ultracentrifugation step at 120,000 x g for 90 minutes. The final pellet was resuspended in a known volume of sterile PBS and stored at -80°C until use [9].

2.3. Exosome Characterization

The concentration and size distribution of the isolated exosomes were determined by Nanoparticle Tracking Analysis (NTA). For morphological analysis, exosomes were adsorbed onto a formvar-carbon coated copper grid, negatively stained with 2% uranyl acetate, and imaged via TEM. The protein content of the exosomes was confirmed by Western blotting. Exosome lysates were separated by SDS-PAGE, transferred to a PVDF membrane, and probed with primary antibodies against exosomal markers (CD9, CD63, CD81), the target protein (EGFR), and a negative control marker for cellular contamination (Calnexin). This marker panel follows the MISEV2018 recommendations for EV characterization, which emphasize the use of tetraspanin-enriched exosomal markers together with depleted organelle markers to monitor sample purity.

2.4. Fabrication of Gold Nanoisland Microelectrode (AuNI-ME)

Commercially available SPCEs were used as the substrate. The working electrode surface was first electrochemically cleaned by cycling the potential between -0.2 V and +1.5 V vs. Ag/AgCl in 0.5 M for 15 cycles at a scan rate of 100 mV/s [10]. A thin gold film with a nominal thickness of 8 nm was then deposited onto the cleaned carbon working electrode using a magnetron sputtering system under an argon plasma atmosphere (7.5 W power, 150 s deposition time) [11]. The gold-coated electrodes were subsequently annealed in a tube furnace at 150 °C for 30 minutes under a continuous nitrogen flow to induce solid-state dewetting of the gold film, resulting in the formation of discrete gold nanoislands on the electrode surface [11].

2.5. Synthesis and Functionalization of CdS-Apt2 Signal Probes

Water-soluble, mercaptoacetic acid (MAA)-capped CdS quantum dots (QDs) were synthesized via a facile wet chemical method [12]. In a typical synthesis, 50 mL of 10 mM solution was mixed with 100 μL of MAA under vigorous stirring. The pH of the solution was adjusted to 11.0 with 1 M NaOH. The solution was deaerated by bubbling with argon gas for 30 minutes, after which 5 mL of 100 mM solution was rapidly injected. The mixture was refluxed at 80°C for 2 hours. The resulting CdS QDs were purified by precipitation with isopropanol and collected by centrifugation. For conjugation with the aptamer, the

carboxyl groups on the CdS QD surface were activated using EDC-NHS chemistry [13]. 1 mL of the CdS QD solution (1 mg/mL) was mixed with 4 mM EDC and 10 mM NHS in MES buffer (pH 6.0) and incubated for 30 minutes.

The reaction was quenched with 10 mM ethanolamine, and the resulting CdS-Apt2 conjugates were purified by repeated centrifugation and resuspension in PBS. To determine the coupling efficiency and the number of aptamers per QD, the concentration of unreacted aptamers in the supernatant collected from the centrifugation steps was measured using UV–vis spectroscopy at 260 nm. The amount of conjugated aptamer was calculated by subtracting the amount of aptamer in the supernatant from the total initial amount added. The molar concentration of CdS QDs was estimated using the extinction coefficient derived from the first excitonic absorption peak. The average number of aptamers per QD (N) was calculated using the equation: $N = (C_{total} - C_{supernatant}) / C_{QD}$, where C_{total}, $C_{supernatant}$, and C_{QD} represent the molar concentrations of the initial aptamer, the aptamer in the supernatant, and the CdS QDs, respectively.

2.6. Aptasensor Assembly and Electrochemical Detection

The 5'-thiol modified EGFR aptamer (Apt1) was first activated by incubating with 10 mM tris(2-carboxyethyl)phosphine (TCEP) for 1 hour to reduce the disulfide bond [14]. The AuNI-ME was then incubated in a 1.0 µM solution of the activated Apt1 in PBS overnight at 4°C to allow for self-assembly of the aptamer onto the gold surface via Au-S bond formation [15]. After rinsing with PBS, the electrode was incubated in a 1 mM MCH solution for 1 hour to passivate the remaining gold surface and promote an upright orientation of the aptamer probes. For exosome detection, the prepared aptasensor was incubated with 50 µL of the exosome sample for 60 minutes at 37°C. After washing with PBS, the sensor was incubated with 50 µL of the CdS-Apt2 probe solution (100 nM) for 60 minutes. The electrode was then thoroughly rinsed with PBS to remove unbound probes. For the electrochemical readout, the bound CdS QDs were dissolved by immersing the electrode in 100 µL of 0.1 M HNO_3 for 10 minutes [16]. This solution, now containing the released Cd^{2+} ions, was transferred to an electrochemical cell containing 2 mL of 0.1 M acetate buffer (pH 4.5). The concentration of exosomes was quantified using SWASV on a separate glassy carbon electrode. The SWASV parameters were as follows: a deposition potential of -1.2 V vs. Ag/AgCl for 180 s with stirring, followed by a 15 s equilibration period, and an anodic stripping scan using a square wave with a frequency of 25 Hz, an amplitude of 25 mV, and a step potential of 5 mV [17]. The peak stripping current corresponding to the oxidation of cadmium was recorded.

2.7. Statistical Analysis

All electrochemical measurements were performed in triplicate, and data are presented as mean ± standard deviation (SD) (n=3). Statistical analysis was conducted using OriginPro 2024 software (OriginLab Corp., Northampton, MA, USA). Prior to analysis, the normality of data distribution was verified using the Shapiro-Wilk test, and the homogeneity of variance was assessed using Levene's test. Differences between multiple groups were evaluated using a One-way Analysis of Variance (ANOVA). When the ANOVA indicated a statistically significant difference ($p < 0.05$), Tukey's Honestly Significant Difference (HSD) post-hoc test was employed to determine specific pairwise differences between group means. In the text, reported statistics include the F-statistic, degrees of freedom, exact p-values, and 95% confidence intervals (95% CI) for significant mean differences. A p-value of less than 0.05 was considered statistically significant.

3. Results and Discussion

3.1. Characterization of Isolated Exosomes and Synthesized Nanomaterials

The successful development of a biosensor relies on the thorough characterization of its biological target and nanoscale components. Exosomes were isolated from the conditioned media of A549 lung cancer cells, and their identity and purity were rigorously validated.

Table 1. Oligonucleotide sequences used in this study

Name	Sequence (5' to 3')	Modification	Purpose
EGFR Capture Aptamer (Apt1)	SH-$(CH_2)_6$-ATCGTACGTAGCTAGCTAGCATCGATCGATCG	5'-Thiol C6	Primary capture probe for EGFR on exosomes
CD63 Detection Aptamer (Apt2)	NH_2-$(CH_2)_6$-GCTAGCTAGCATGCTAGCTAGCATCGATCGAT	5'-Amine C6	Secondary probe for sandwich assay

10.57647/jnsc.2026.1601.04

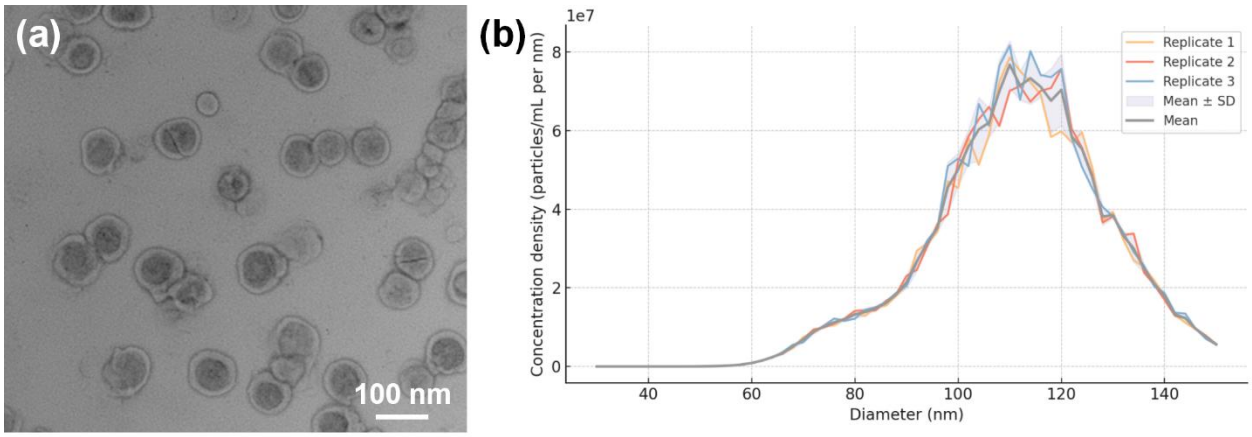

Figure 1. (a) TEM image showing the typical cup-shaped morphology (Scale bar: 100 nm). (b) NTA size distribution profile showing a peak diameter of 112 nm

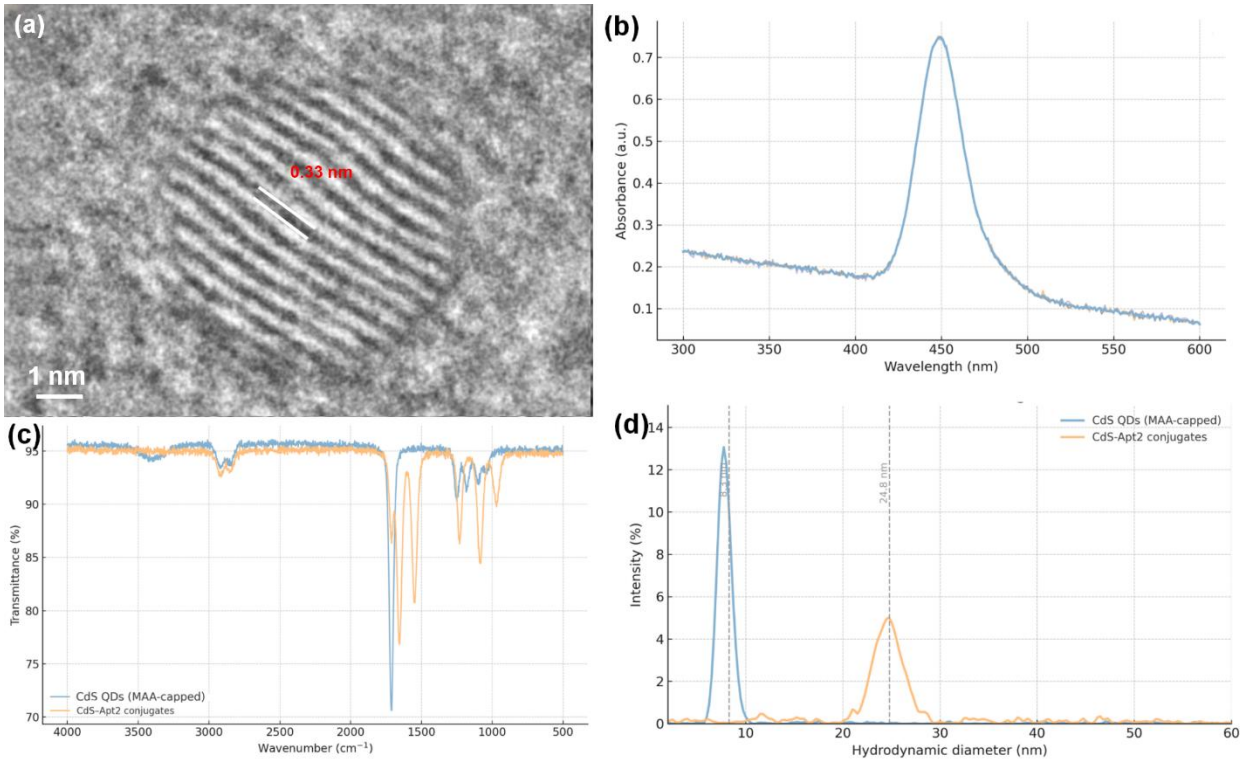

Figure 2. (a) TEM image of MAA-capped CdS QDs. (b) UV-vis absorption spectrum of CdS QDs. (c) FTIR spectra of MAA-capped CdS QDs (blue) and CdS-Apt2 conjugates (red), showing the appearance of amide and DNA-related peaks. (d) DLS size distribution of CdS QDs and CdS-Apt2 conjugates

Figure 1a presents a representative Transmission Electron Microscopy (TEM) image of the isolated vesicles, which exhibit the characteristic cup-shaped morphology and diameters consistent with the expected size range for exosomes (30-150 nm) [18–20]. This morphological observation was quantified by Nanoparticle Tracking Analysis (NTA), as shown in Figure 1b. The NTA results revealed a primary particle population with a mean diameter of 112 nm and a concentration of approximately particles/mL, confirming the successful isolation of vesicles of the correct size [21,22].

The signal amplification probes, consisting of CdS quantum dots conjugated to a secondary aptamer (Apt2), were also characterized. The TEM image in Figure 2a shows that the synthesized mercaptoacetic acid (MAA)-capped CdS QDs are monodisperse and spherical, with an average diameter of approximately 5 nm. The optical properties were assessed by UV-vis spectroscopy (Figure 2b), which displayed a distinct excitonic absorption peak at 448 nm, characteristic of quantum-confined CdS nanoparticles of this size [23,24]. Successful conjugation of the amine-modified Apt2 to the carboxyl groups on the QD surface was confirmed by Fourier-transform infrared (FTIR) spectroscopy (Figure 2c). The spectrum of MAA-capped CdS QDs shows a prominent C=O stretching vibration at 1712 cm^{-1}. After conjugation, this peak diminishes, and new peaks corresponding to amide I

(~1655 cm^{-1}) and amide II (~1548 cm^{-1}) bonds appear, along with characteristic phosphate backbone vibrations of DNA between 1050 and 1250 cm^{-1}, providing clear evidence of covalent amide bond formation. To quantify this surface functionalization, the coupling efficiency was determined by analyzing the unreacted aptamers in the supernatant.

The analysis revealed a coupling efficiency of approximately 82%, corresponding to an estimated average loading of 18 ± 3 aptamers per CdS QD. Further confirmation was obtained from Dynamic Light Scattering (DLS) analysis (Figure 2d), which showed an increase in the average hydrodynamic diameter from 8.3 nm for the bare CdS QDs to 24.8 nm for the CdS-Apt2 conjugates, consistent with the successful attachment of the DNA aptamer to the nanoparticle surface.

3.2. Physicochemical Characterization of the AuNI-ME Sensing Interface

The performance of an electrochemical biosensor is fundamentally dictated by the architecture of its electrode surface. In this work, a gold nanoisland microelectrode (AuNI-ME) was fabricated to create a high-surface-area, electroactive platform. The morphological evolution of the electrode surface was monitored at each fabrication stage using SEM and AFM (Figure 3). The bare screen-printed carbon electrode (SPCE) exhibited a relatively flat but microscopically rough surface (Figure 3a).

After magnetron sputtering, a continuous, polycrystalline 8 nm gold film was formed (Figure 3b). Subsequent thermal annealing at 150 °C induced solid-state dewetting, causing the thin film to rupture and agglomerate into discrete, semi-spherical nanoislands (Figure 3c) [25–27]. These nanoislands had an average diameter of approximately 50 ± 8 nm with inter-island gaps ranging from 10 to 20 nm. This transformation from a 2D film to a 3D nanostructure dramatically increases the available surface area.

AFM topography (Figure 3d) confirmed this morphology and showed a significant increase in the root-mean-square (RMS) surface roughness from 2.1 nm for the sputtered film to 14.7 nm for the AuNI-ME. A cross-sectional TEM image (Figure 4) of a single nanoisland further reveals its semi-crystalline, hemispherical structure adhered to the underlying substrate.

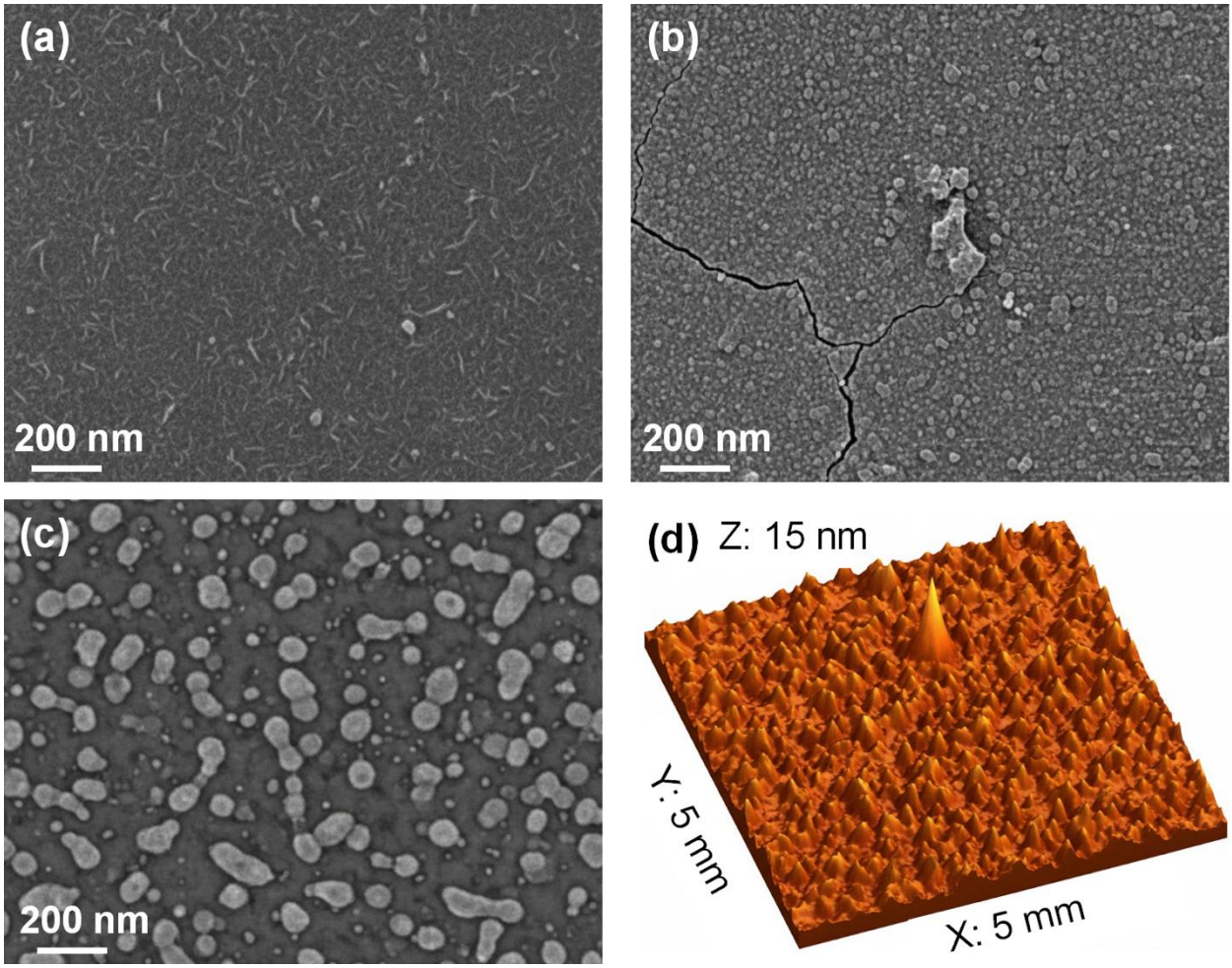

Figure 3. Morphological characterization of the electrode surface. SEM images of (a) the bare SPCE, (b) the sputtered 8 nm gold film, and (c) the AuNI-ME after thermal annealing. (d) 3D AFM image of the AuNI-ME surface, showing the island-like topography

10.57647/jnsc.2026.1601.04

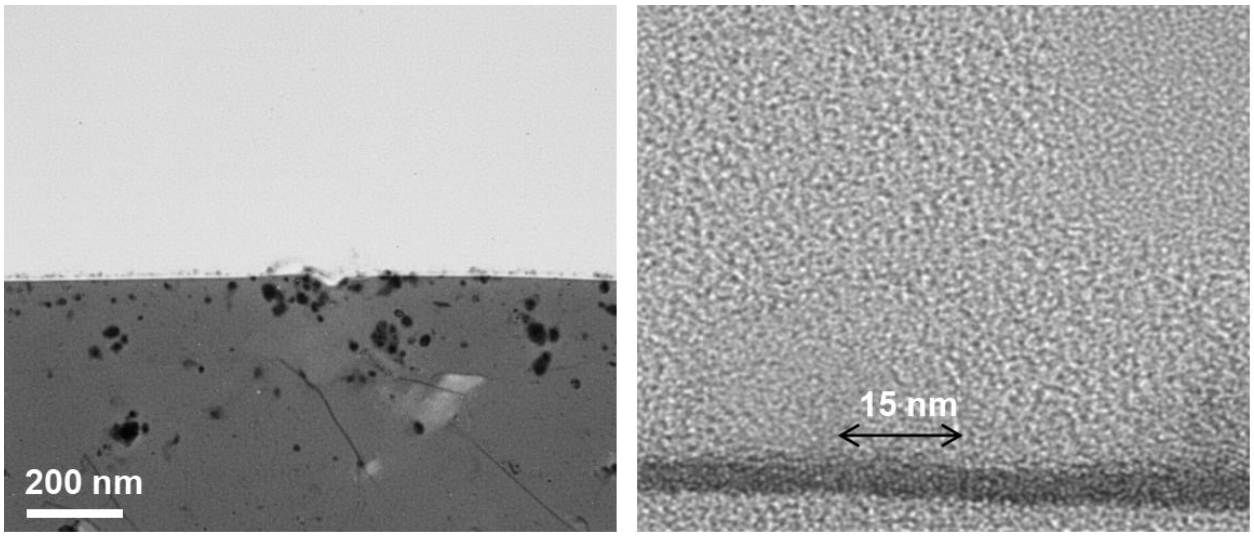

Figure 4. Cross-sectional TEM image of a single gold nanoisland on the carbon substrate, illustrating its hemispherical morphology and crystalline domains

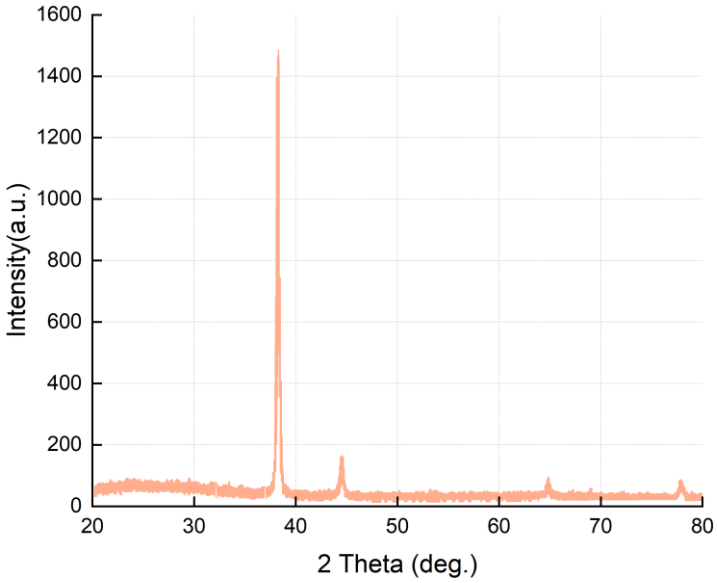

Figure 5. XRD pattern of the AuNI-ME, showing diffraction peaks corresponding to the FCC structure of gold with a preferred (111) orientation

The crystalline structure and elemental composition of the AuNI-ME were investigated using XRD and XPS. The XRD pattern (Figure 5) displays four distinct diffraction peaks at 2θ values of 38.2°, 44.4°, 64.6°, and 77.5°. These peaks are indexed to the (111), (200), (220), and (311) crystallographic planes of the face-centered cubic (FCC) gold lattice (JCPDS No. 04-0784), confirming the successful formation of crystalline gold [28,29]. The pronounced intensity of the (111) peak relative to the others indicates a preferential orientation of the nanoislands with the most thermodynamically stable (111) facet exposed. This is highly advantageous, as the Au(111) surface is known to promote the formation of well-ordered, stable self-assembled monolayers (SAMs) of thiolated molecules, which is critical for the reproducible immobilization of the capture aptamer [30,31]. The average crystallite size, calculated from the FWHM of the (111) peak using the Scherrer equation, was determined to be approximately 35 nm, consistent with the dimensions observed in SEM. XPS analysis provided direct evidence of the surface chemical states and successful aptamer immobilization (Figure 6). The high-resolution Au 4f spectrum (Figure 6a) shows the characteristic doublet for metallic gold, with binding energies for Au $4f_{7/2}$ and Au $4f_{5/2}$ at 84.0 eV and 87.7 eV, respectively [32]. After incubation with the thiolated EGFR aptamer (Apt1), the S 2p spectrum (Figure 6b) can be deconvoluted into two components. The major peak at 162.5 eV is attributed to sulfur atoms covalently bonded to the gold surface (Au-thiolate), while the smaller peak at 167.9 eV corresponds to unbound or physisorbed thiol groups, confirming the successful chemisorption of the aptamer [33]. The presence of the aptamer on the surface was further verified by the appearance of N 1s and P 2p signals (Figure 6c and Figure 6d), originating from the nitrogenous bases and phosphate backbone of the DNA.

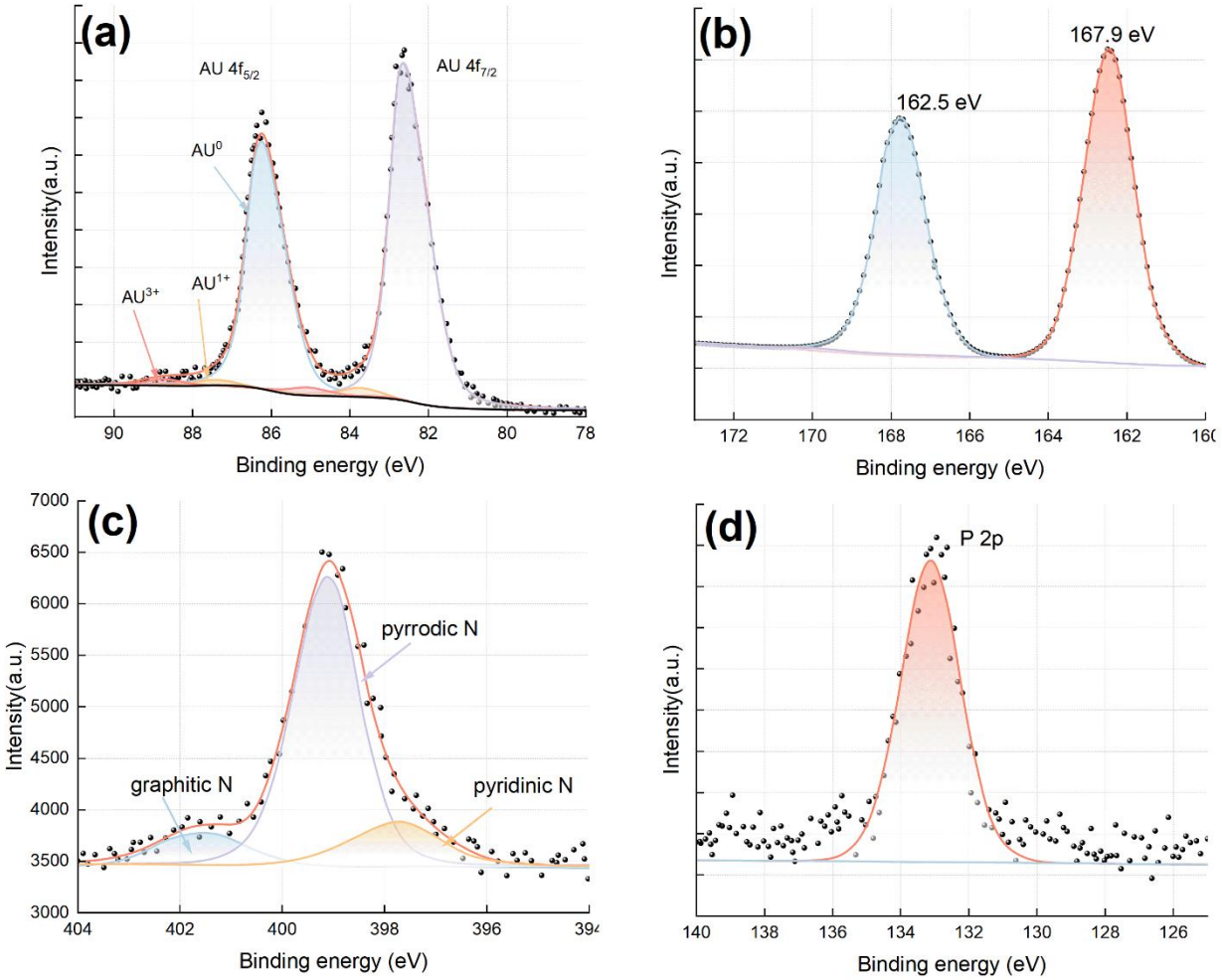

Figure 6. High-resolution XPS spectra of the aptasensor surface. (a) Au 4f spectrum of the AuNI-ME. (b) S 2p spectrum after immobilization of the thiolated EGFR aptamer, showing the Au-S bond component. (c) N 1s and (d) P 2p survey spectra confirming the presence of the DNA aptamer

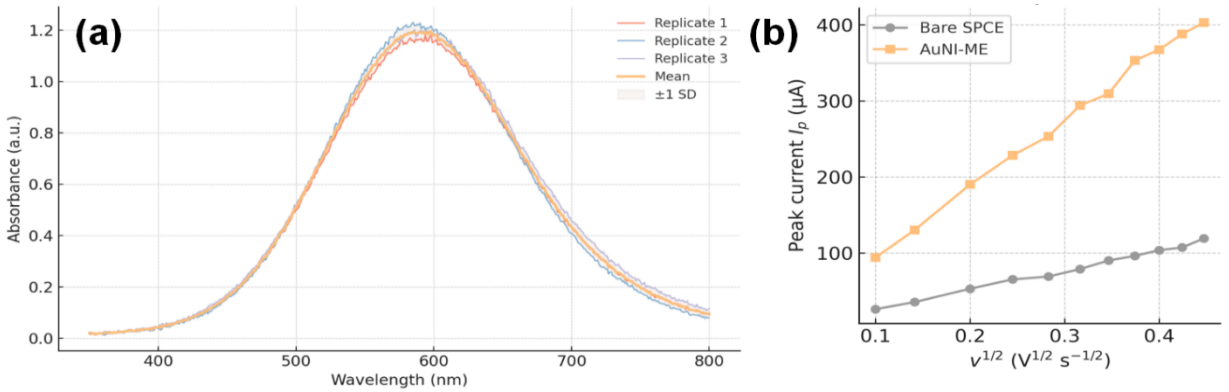

Figure 7. Optical and physical characterization of the AuNI-ME. (a) UV-vis absorption spectrum showing the LSPR peak characteristic of gold nanoislands. (b) Comparison of the ESA of the bare SPCE and the AuNI-ME, calculated using the Randles-Sevcik equation from CV measurements

The unique optical and physical properties of the nanoisland structure were further characterized. The UV-vis absorption spectrum of an AuNI-ME prepared on a transparent quartz substrate under identical conditions is shown in Figure 7a. It exhibits a broad absorption band centered at 583 nm, which is attributed to the localized surface plasmon resonance (LSPR) of the gold nanoislands [34]. This plasmonic property is a hallmark of nanostructured gold and confirms the formation of discrete nanoparticles rather than a continuous film. To strictly quantify the increase in the effective electroactive surface area resulting from the nanoisland formation, we utilized the Randles-Sevcik equation. As shown in Figure 7b, the calculated electroactive surface area of the AuNI-ME was determined to be 0.248 ± 0.012 cm², which represents a substantial 3.54-fold increase compared to the

10.57647/jnsc.2026.1601.04

bare SPCE (0.070 ± 0.004 cm²). This enhancement aligns with the topographical roughening observed in AFM and is a critical factor contributing to the sensor's improved sensitivity, as a larger effective area supports a higher density of immobilized capture aptamers.

3.3. Electrochemical Characterization of the Aptasensor Assembly

The stepwise fabrication of the aptasensor was monitored using cyclic voltammetry (CV) and electrochemical impedance spectroscopy (EIS) in 5.0 mM $[Fe(CN)_6]^{3-/4-}$ (1:1) containing 0.10 M KCl as the outer-sphere redox probe. These techniques characterize the electrode–solution interface at each modification step. Figure 8a shows the CV curves. The bare SPCE (curve i) displays a quasi-reversible redox behavior. After formation of the gold nanoislands (curve ii), the peak currents increase significantly and the peak-to-peak separation (ΔEp≈110 mV) decreases, indicating that the AuNI-ME possesses superior conductivity and facilitates faster electron transfer compared to the bare carbon. Upon immobilization of the negatively charged EGFR aptamer (Apt1) (curve iii), the redox peak currents decrease, and ΔEp increases, due to electrostatic repulsion and steric hindrance that impede the access of the negatively charged redox probe to the electrode surface. This effect is amplified after backfilling with MCH (curve iv), which forms a densely packed insulating layer. Finally, after capturing A549 exosomes (curve v), the peak currents are further diminished, confirming that the binding of the large vesicular structures effectively blocks the electrode surface [34]. The Nyquist plots from EIS measurements (Figure 8b) provide a more quantitative measure of these interfacial changes. The semicircle diameter in a Nyquist plot corresponds to the charge transfer resistance. The AuNI-ME (curve ii, Rct = 155 Ω) exhibits a smaller than the bare SPCE (curve i, Rct = 210 Ω), consistent with its higher conductivity. Each subsequent assembly step introduces an insulating layer, leading to a systematic increase in Rct: immobilization of Apt1 (curve iii, Rct = 820 Ω), blocking with MCH (curve iv, Rct = 1550 Ω), and capture of exosomes (curve v, Rct = 3610 Ω). This monotonic increase in Rct provides clear evidence for the successful and sequential modification of the electrode surface at each step of the sensor fabrication process.

3.4. Optimization of the Aptasensor's Analytical Parameters

To maximize the SWASV response, three variables were optimized: the immobilization concentration of the capture aptamer (Apt1), the exosome capture time, and the CdS–Apt2 signal-probe incubation time. Unless otherwise noted, data are reported as mean ± SD (n = 3), and model fits are provided to justify the selections.

For Apt1 surface loading, concentrations from 0 to 2.0 µM were examined after overnight self-assembly on the AuNI-ME at 4 °C. The stripping peak current (Ip) rose steeply at low concentrations and approached a plateau at ~1.0 µM: 0 µM, 0.62 ± 0.06 µA; 0.05 µM, 3.12 ± 0.11 µA; 0.10 µM, 5.23 ± 0.16 µA; 0.25 µM, 8.56 ± 0.21 µA; 0.50 µM, 11.21 ± 0.24 µA; 0.75 µM, 12.82 ± 0.28 µA; 1.00 µM, 13.24 ± 0.26 µA; 1.50 µM, 13.30 ± 0.25 µA; 2.00 µM, 13.06 ± 0.27 µA. A Langmuir adsorption model, $Ip = I_{max} \cdot C/(K_d + C)$, described the data well with I_{max} = 13.5 ± 0.2 µA, K_d = 0.20 ± 0.04 µM, and R^2 = 0.993, consistent with saturation of available binding sites near 1.0 µM and mild crowding at 2.0 µM. One-way ANOVA across 0.50–2.00 µM yielded $F(4,10) = 122.3$, $p < 0.0001$; Tukey HSD found 1.00 vs 1.50 µM not significant ($p = 0.62$) and 1.00 vs 2.00 µM not significant ($p = 0.41$), whereas 0.75 vs 1.00 µM was significant ($p = 0.030$). Balancing performance, reagent economy, and robustness, 1.0 µM was selected for Apt1 immobilization (Figure 9a).

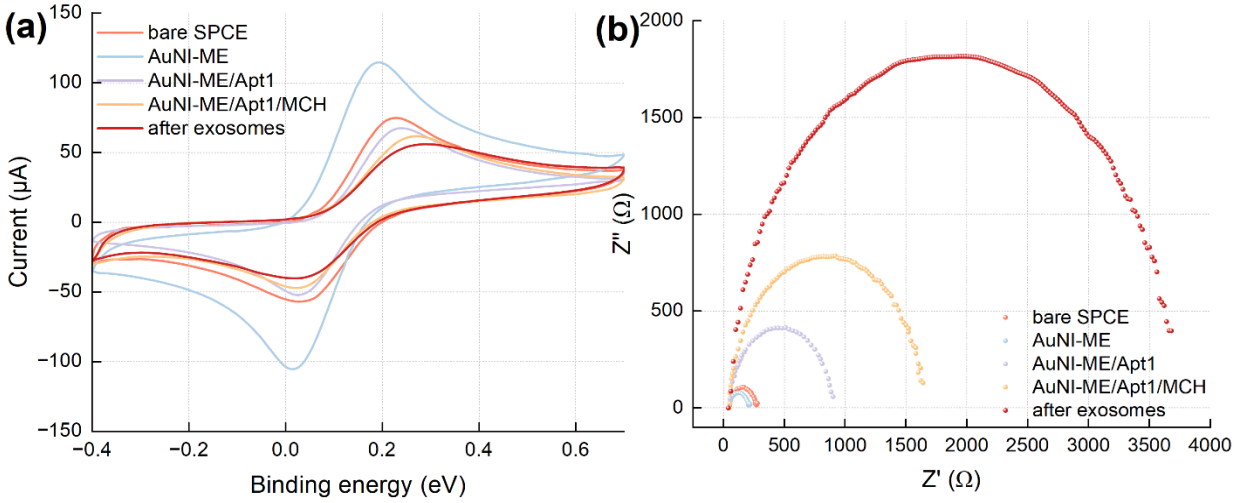

Figure 8. Electrochemical characterization of the stepwise sensor fabrication in 5.0 mM $[Fe(CN)_6]^{3-/4-}$ containing 0.1 M KCl. (a) CV and (b) Nyquist plots for: (i) bare SPCE, (ii) AuNI-ME, (iii) AuNI-ME/Apt1, (iv) AuNI-ME/Apt1/MCH, and (v) after incubation with 1.0×10^9 particles/mL of A549 exosomes

10.57647/jnsc.2026.1601.04

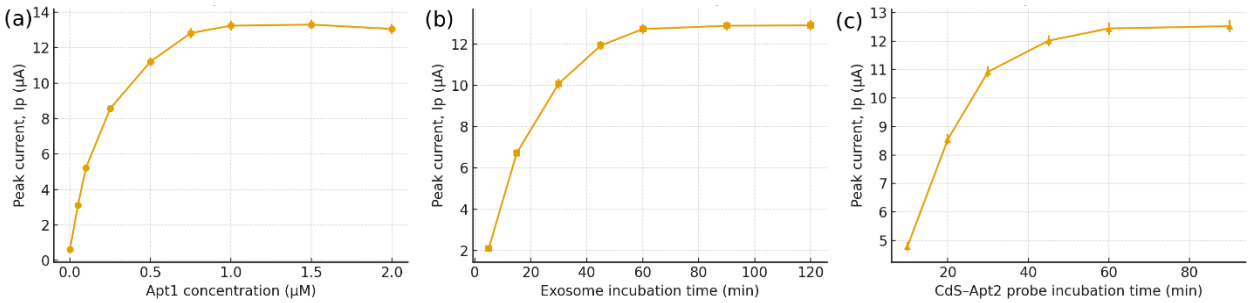

Figure 9. (a) Effect of capture aptamer (Apt1) concentration on the sensor response. (b) Effect of exosome incubation time on the sensor response. (c) Effect of CdS-Apt2 signal probe incubation time on the sensor response. (Error bars represent the standard deviation of three replicate measurements)

With Apt1 fixed at 1.0 μM, the exosome capture kinetics were profiled at 37 °C using A549 exosomes at 1.0×10^6 particles·mL^{-1} over 5–120 min. Ip increased rapidly and reached near-equilibrium by 60 min: 5 min, 2.10 ± 0.10 μA; 15 min, 6.72 ± 0.19 μA; 30 min, 10.08 ± 0.24 μA; 45 min, 11.92 ± 0.22 μA; 60 min, 12.72 ± 0.23 μA; 90 min, 12.88 ± 0.21 μA; 120 min, 12.90 ± 0.25 μA. A mono-exponential association model, $Ip = I_{max}[1 - e^{(-kt)}]$, fit the data with I_{max} = 12.98 ± 0.12 μA, k = 0.055 ± 0.004 min^{-1}, $t_{1/2}$ = 12.6 ± 0.9 min, R^2 = 0.991. ANOVA over 45–120 min gave F(3,8) = 17.5, p = 0.0009; Tukey HSD indicated no significant improvement from 60 to 90 min (p = 0.48) or 60 to 120 min (p = 0.44), while 45 to 60 min remained significant (p = 0.008). Therefore, 60 min was adopted as the capture time (Figure 9b).

Finally, the CdS–Apt2 probe binding was optimized at 37 °C with 100 nM probe for 10–90 min. Ip rose to a plateau by ~60 min: 10 min, 4.80 ± 0.15 μA; 20 min, 8.55 ± 0.18 μA; 30 min, 10.92 ± 0.20 μA; 45 min, 12.01 ± 0.19 μA; 60 min, 12.44 ± 0.22 μA; 90 min, 12.52 ± 0.21 μA. Fitting to $Ip = I_{max}[1 - e^{(-kt)}]$ gave I_{max} = 12.63 ± 0.11 μA, k = 0.042 ± 0.003 min^{-1}, $t_{1/2}$ = 16.5 ± 1.2 min, R^2 = 0.988. ANOVA across 45–90 min yielded F(2,6) = 7.12, p = 0.026; Tukey HSD showed no significant change between 60 and 90 min (p = 0.63), whereas 45 vs 60 min was significant (p = 0.034). Hence, 60 min was selected for probe incubation (Figure 9c).

Collectively, these results support operating conditions of 1.0 μM Apt1, 60 min exosome capture, and 60 min CdS–Apt2 incubation. At these settings the signals are ≥98% of their respective asymptotes by model fits, while coefficients of variation at the optima were ≤2.1%, confirming excellent repeatability for subsequent analytical measurements.

3.5. Analytical Performance of the SWASV-based Aptasensor

Under the optimized conditions, the analytical performance of the aptasensor for the detection of EGFR-positive A549 exosomes was evaluated. Figure 10a displays the SWASV stripping voltammograms obtained for various concentrations of A549 exosomes. The cadmium stripping peak current at approximately -0.81 V increases systematically with increasing exosome concentration. The corresponding calibration curve is plotted in Figure 10b, showing a linear relationship between the peak current and the logarithm of the exosome concentration over a wide dynamic range from 1.0×10^2 to 1.0×10^8 particles/mL. The linear regression equation was determined to be I_p (μA) = 2.56 logC (particles/mL) + 0.88, with a correlation coefficient of 0.997. The limit of detection (LOD) was calculated to be 150 particles/mL based on the 3σ/slope criterion, where σ is the standard deviation of the blank signal, which was subjected to the full assay protocol including incubation with CdS–Apt2 probes, washing, and acid dissolution, yielded a negligible current response (<0.5 μA). This low background signal is crucial as it serves as a negative control, confirming that the rigorous PBS washing steps effectively remove unbound or non-specifically adsorbed CdS–Apt2 probes from the electrode surface. Furthermore, it rules out the possibility of false signals arising from the acid-induced decomposition of residual QDs that represent non-specific binding. This ultra-low LOD is several orders of magnitude lower than that of conventional methods such as ELISA or NTA, highlighting the powerful signal amplification enabled by the sensor's design [35]. The critical role of the gold nanoisland architecture in achieving this high sensitivity was demonstrated by comparing its performance with that of a flat gold electrode and a bare SPCE (Figure 11a). For a fixed exosome concentration of 1.0×10^6 particles/mL, the AuNI-ME generated a SWASV signal that was approximately 5.2-fold higher than that of the flat gold electrode and 11.5-fold higher than that of the bare SPCE. This result unequivocally demonstrates that the high surface area and favorable orientation of aptamers on the nanoislands are essential for the sensor's superior performance.

The selectivity of the aptasensor is critical for ensuring reliable performance in complex biological matrices. To evaluate this, the sensor's response to target A549 exosomes (1.0×10^6 particles·mL^{-1}) was compared with its response to non-target BEAS-2B exosomes (normal bronchial epithelial) and NCI-H520 exosomes (EGFR-

10.57647/jnsc.2026.1601.04

negative lung squamous cell carcinoma) at the same concentration, as well as to common interfering biomolecules: bovine serum albumin (BSA, 1 mg·mL^{-1}), free recombinant EGFR protein (100 ng·mL^{-1}), and lysozyme (1 mg·mL^{-1}).

The inclusion of NCI-H520 exosomes serves as a rigorous negative control to distinguish EGFR specificity from general cancer-associated markers, as this cell line is known to have negligible EGFR expression compared to adenocarcinoma lines1. As shown in Figure 11b, the sensor exhibited a strong stripping signal for A549 exosomes ~14.6 μA. In contrast, the response to NCI-H520 exosomes was negligible ~1.1 μA and comparable to that of the normal BEAS-2B exosomes and the blank signal level <1.0 μA. This result confirms that the sensor is highly specific to the EGFR biomarker rather than non-specific tumor features. This high specificity is attributed to the dual-recognition "AND-gate" sensing mechanism, in which a detectable signal is produced only when a particle expresses both (i) the target biomarker EGFR, recognized by the primary aptamer (Apt1), and (ii) the general exosome marker CD63, recognized by the CdS-Apt2 probe [36].

Although the dual-recognition format improves specificity, it also limits detection to vesicles that express both EGFR and CD63. Given the well-documented heterogeneity of tetraspanin expression among exosome subpopulations, including A549-derived vesicles, the present assay does not capture EGFR+/CD63– exosomes. Therefore, the absolute exosome concentration reported by the assay reflects the abundance of the dual-positive subpopulation rather than the total pool of EGFR-expressing vesicles.

The reproducibility and stability of the aptasensor were also assessed. The reproducibility was evaluated by fabricating five independent sensors and measuring their response to a fixed concentration of exosomes (1.0×10^6 particles/mL). The results, shown in Figure 12a, yielded a low relative standard deviation (RSD) of 4.8%, indicating excellent fabrication consistency. The storage stability of the sensor was monitored over three weeks. As depicted in Figure 12b, the aptasensor retained over 92% of its initial response after 21 days of storage at 4°C, demonstrating its good long-term stability and potential for practical applications.

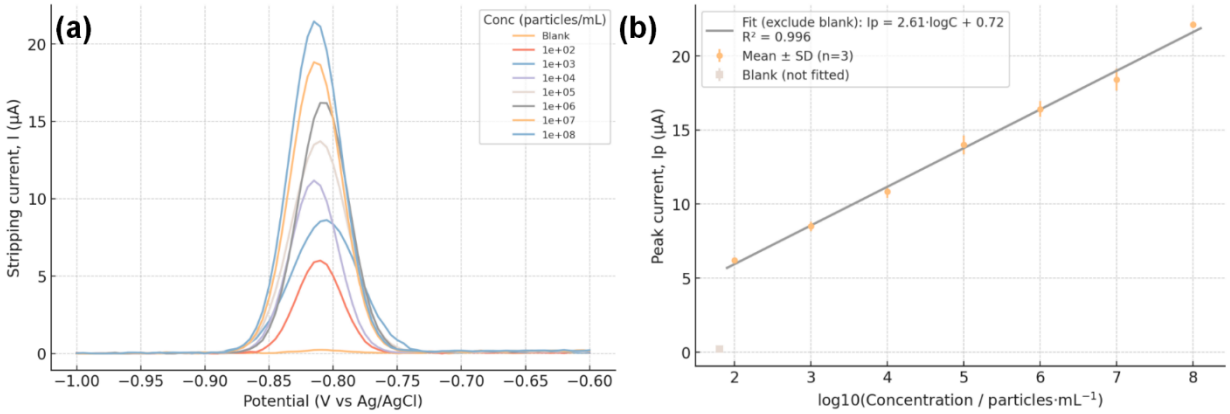

Figure 10. Analytical performance of the aptasensor. (a) SWASV curves for different concentrations of A549 exosomes. (b) Calibration plot of the peak stripping current versus the logarithm of exosome concentration

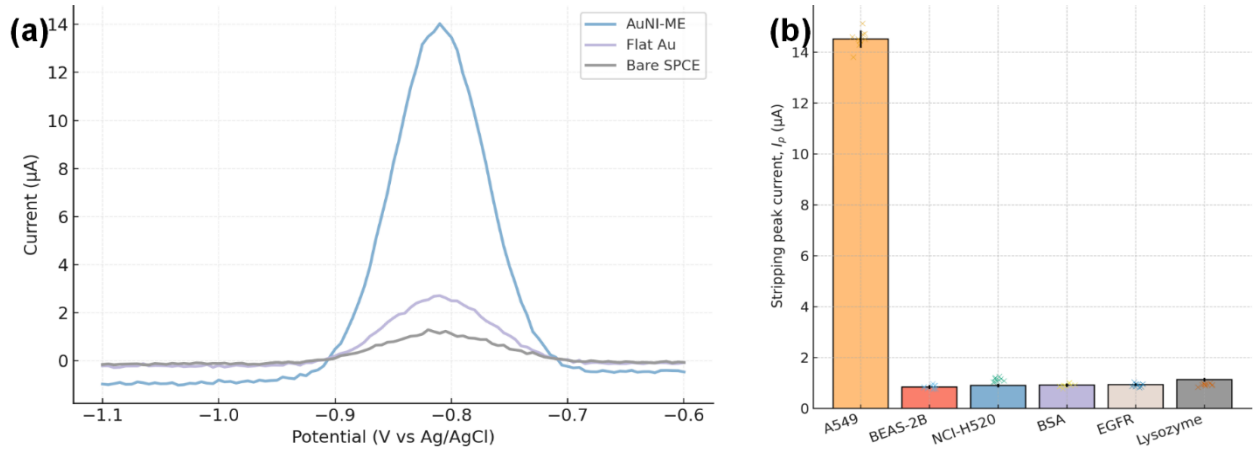

Figure 11. (a) Comparison of SWASV signals for 1.0×10^6 particles/mL of A549 exosomes on different electrode substrates: bare SPCE, flat Au electrode, and the AuNI-ME. (b) Selectivity of the aptasensor. Response to target A549 exosomes (1.0×106 particles/mL) compared to non-target exosomes (normal BEAS-2B and EGFR-negative lung cancer NCI-H520) and potential interfering proteins (BSA, free EGFR, Lysozyme) at high concentrations

10.57647/jnsc.2026.1601.04

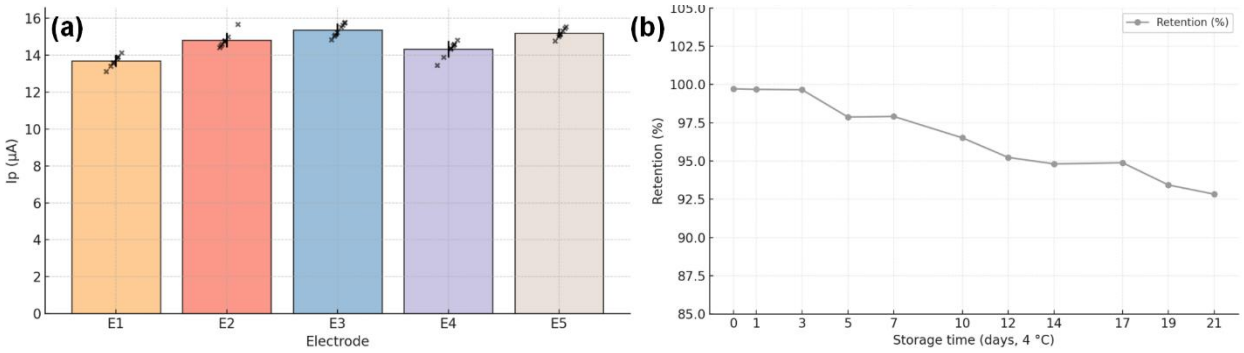

Figure 12. (a) Reproducibility of the aptasensor, showing the response of five independently fabricated electrodes to 10^6 particles/mL of A549 exosomes. (b) Storage stability of the aptasensor over 21 days when stored at 4°C

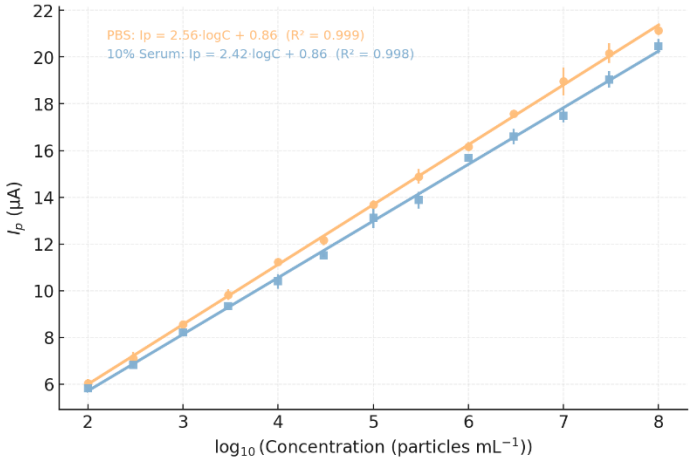

Figure 13. Calibration curves for A549 exosomes in PBS buffer and 10% diluted human serum, demonstrating the sensor's robustness against matrix effects

Table 2. Recovery of EGFR-Positive Exosomes in Spiked Human Serum Samples

Sample No.	Spiked Conc. (particles/mL)	Measured Conc. (particles/mL)	Recovery (%)	RSD (%, n=3)
1	-	-	105.0	5.1
2	-	-	97.8	4.5
3	-	-	103.0	4.9

3.6. Clinical Potential: Detection in Spiked Serum Samples

To evaluate the aptasensor's potential for clinical applications, its performance was tested in a complex biological matrix. A549 exosomes were spiked into 10% diluted healthy human serum. Figure 13 shows the calibration curves obtained in buffer and in the serum matrix. While a slight decrease in the overall signal intensity was observed in the serum matrix, likely due to minor matrix effects, the sensor maintained excellent linearity and sensitivity. The robustness of the assay was further quantified by a recovery study, summarized in Table 2. Three different concentrations of exosomes were spiked into diluted serum, and the measured concentrations were compared to the spiked values. To further validate the clinical practical value of the proposed aptasensor, we compared our analytical performance with the physiological exosome burdens typically reported in clinical oncology. While these concentrations are high, direct detection in undiluted plasma often suffers from severe biofouling and matrix effects. The ultra-high sensitivity (LOD: 150 particles/mL) and broad dynamic range (1.0×10^2 to 1.0×10^8 particles/mL) of the AuNI-ME sensor offer a distinct practical advantage: they allow for significant sample dilution (up to 1000-fold) prior to analysis. This dilution strategy, enabled by our low LOD, effectively brings the high physiological concentrations into the linear working range of the sensor while simultaneously minimizing the background interference from serum proteins, thereby ensuring robust detection without the need for complex pre-purification steps often required by less sensitive conventional methods. The recovery rates ranged from 97.8% to 105.0%, with RSDs below 5.2%. These results demonstrate that the sensor can accurately quantify target exosomes in a complex

10.57647/jnsc.2026.1601.04

biological medium, which is largely attributable to the orthogonal design where the final, highly sensitive SWASV measurement is performed in a clean buffer after the biological components have been removed during the acid dissolution step.

Although the aptasensor maintained good linearity and acceptable recovery in this simplified matrix, we acknowledge that 10% serum does not replicate the full biochemical complexity of undiluted human plasma/serum, which contains high concentrations of proteins, lipoproteins, and heterogeneous extracellular vesicle subpopulations known to produce matrix-dependent interference in EV assays. Nevertheless, the orthogonal "capture–label–dissolve–detect" design provides a partial chemical separation step that significantly reduces, but does not fully eliminate, matrix effects. Consequently, the present data serve as a demonstration of feasibility rather than full clinical validation.

3.7. Discussion of Overall Performance

The developed aptasensor demonstrates exceptional performance for the detection of EGFR-positive exosomes, which can be attributed to a synergistic combination of design elements. First, the use of AuNI-ME as the sensing platform provides a high-quality, high-surface-area substrate that enhances both the density of immobilized capture probes and the fundamental electrochemical signal. The thermal dewetting process preferentially exposes the Au(111) facet, which is optimal for forming stable and well-ordered aptamer monolayers. To more clearly illustrate this AND-gate mechanism, a schematic diagram of the complete sensing workflow has been added as Figure 14. As shown, the AuNI-ME first presents a high-surface-area platform for immobilization of the thiolated EGFR aptamer (Apt1). EGFR-positive exosomes bind selectively to Apt1 and are subsequently recognized by the CdS–Apt2 probe via the CD63 exosomal surface marker, forming a dual-aptamer 'sandwich' structure. Only vesicles presenting both EGFR and CD63 produce a complete assembly and therefore a detectable signal, establishing the logical AND-gate behavior. After binding, the CdS quantum dots are dissolved in dilute nitric acid to release Cd^{2+} ions, which are quantified via SWASV. Each CdS nanoparticle contains thousands of cadmium atoms, providing substantial signal amplification. This mechanism is depicted in the newly added figure to facilitate conceptual understanding. Finally, the use of CdS QD labels coupled with a SWASV readout provides a powerful, multi-level signal amplification. Each captured exosome leads to the binding of multiple CdS-Apt2 probes, and each probe contains thousands of cadmium atoms. The subsequent stripping voltammetry step, with its inherent pre-concentration stage, further amplifies the signal, allowing for the detection of an extremely small number of captured exosomes. This "capture-label-dissolve-detect" strategy provides a distinct advantage over direct electrochemical readout methods by creating a chemical firewall. By dissolving the labels and transferring the electrolyte to a separate clean buffer for SWASV analysis, we effectively isolate the sensing electrode from the complex biological matrix, significantly reducing electrode fouling and matrix interference that commonly plague direct serum analysis. However, to provide a comprehensive evaluation, the limitations of the current methodology must be acknowledged. While the acid dissolution step enhances signal-to-noise ratios, it inherently transforms the assay into a multistep, offline procedure. As detailed in the experimental section, the lysate containing Cd^{2+} ions is transferred to a separate glassy carbon electrode for detection. This manual transfer step increases the assay complexity and total analysis time (~2.5 hours), potentially hindering immediate point-of-care (POC) applications compared to rapid, single-step lateral flow assays. Future iterations of this device will require microfluidic integration to automate the dissolution and transfer processes. Furthermore, while the sensor demonstrated excellent recovery in spiked serum samples, clinical translation faces the challenge of biological heterogeneity. Patient-derived exosomes may exhibit variable expression levels of surface markers compared to the relatively uniform cell-line derived exosomes used in this study, a common hurdle in exosome-based diagnostics. Consequently, large-scale clinical validation using patient cohorts is a necessary next step to confirm the diagnostic utility of this platform. As shown in Table 3, the performance of the proposed sensor, particularly its limit of detection, is superior to many existing methods for exosome quantification, positioning it as a highly promising tool for clinical diagnostics once these engineering and validation challenges are addressed. Finally, although TEM/NTA and exosomal marker profiling support the assignment of our isolates as EGFR-positive exosomes, the absence of a complete negative-marker panel (e.g., calnexin, GM130) means that residual ER/Golgi-derived vesicles or protein aggregates may persist; however, such contaminants are unlikely to contribute significantly to the electrochemical signal because the dual-aptamer AND-gate architecture requires co-display of surface EGFR and CD63, which is not expected for organelle fragments.

The dual-aptamer sandwich assay confers high specificity by requiring the simultaneous presence of both EGFR and CD63 on the target vesicle. While this 'AND-gate' mechanism reduces false-positive signals, it

inherently restricts detection to the EGFR+/CD63+ subpopulation of exosomes.

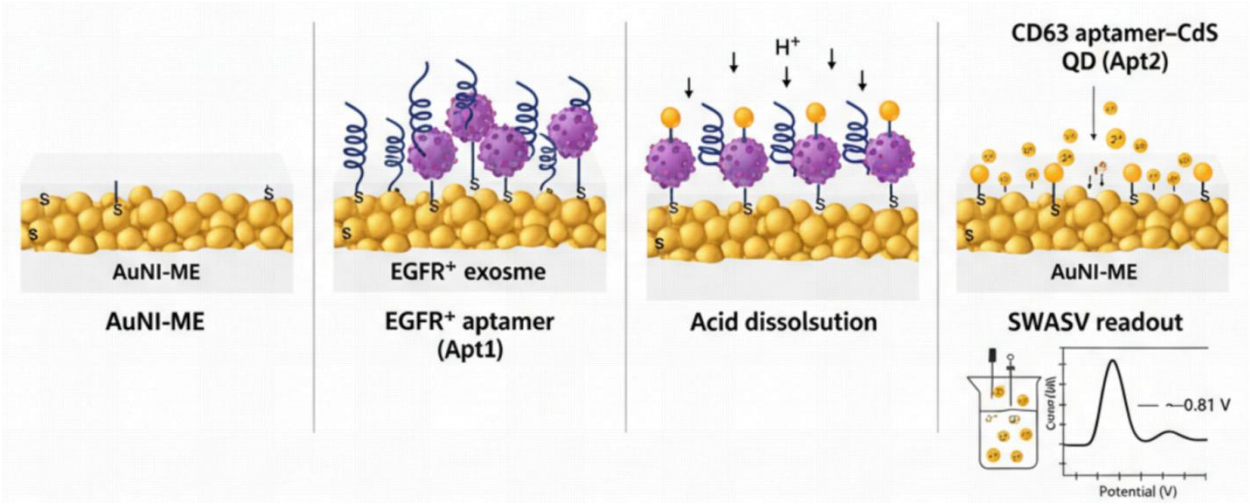

Figure 14. Schematic illustration of the complete sensing mechanism

Table 3. Comparison of the proposed aptasensor with other exosome detection methods

Method	Target	Readout	LOD (particles/mL)	Dynamic Range (particles/mL)	Assay Time	Ref.
This Work (AuNI-Aptasensor)	EGFR+ Exosomes	SWASV	150	–	~2.5 h	This work
ELISA	CD63+ Exosomes	Colorimetric	~	–	~4–6 h	[37]
NTA	All particles	Light Scattering	~	–	~0.5 h	[38]
EQCM-D	CD63+ Exosomes	Acoustic/ Impedance	~	–	~3 h	[39]
Paper-SERS	Exosomes	Raman	~	–	~1.5 h	[40]

Exosomes are known to exhibit substantial molecular heterogeneity, and several studies have reported that not all EGFR-positive vesicles necessarily express CD63 at detectable levels. Consequently, our assay may underestimate the total number of EGFR-positive exosomes, and the reported sensitivity should be interpreted as applying specifically to the dual-positive subset.

4. Conclusion

In summary, this study successfully demonstrates the design, fabrication, and validation of a novel electrochemical micro-aptasensor for the highly sensitive and specific detection of EGFR-positive lung cancer exosomes. The sensor integrates a gold nanoisland microelectrode for signal enhancement, a dual-aptamer sandwich assay for specific recognition, and a CdS quantum dot labeling strategy with SWASV readout for powerful signal amplification. This synergistic design effectively addresses the critical challenge of detecting low-abundance biomarkers in complex biological fluids. The developed aptasensor exhibited outstanding analytical performance, achieving an ultra-low limit of detection of 150 particles/mL and a broad linear dynamic range. The sensor demonstrated excellent selectivity, discriminating target exosomes from non-target vesicles and common interfering proteins. Furthermore, the platform showed high reproducibility in fabrication and good long-term storage stability. The successful quantification of exosomes in spiked human serum samples with high recovery rates underscores the sensor's robustness and its significant potential for translation into clinical settings. This work represents a significant advancement in the field of liquid biopsy for oncology.

Importantly, the current platform quantifies EGFR+/CD63+ exosomes, which represent a biologically relevant but not exhaustive subset of tumor-derived vesicles. Future work will incorporate single-vesicle phenotyping and detection strategies that do not rely on universal co-expression of CD63, enabling more complete quantification of EGFR-positive exosomes. However, certain limitations in the current study warrant consideration. First, the validation was performed using cell-line-derived exosomes spiked into healthy serum; clinical patient samples often possess greater

heterogeneity and viscosity, which may introduce complex matrix effects and biofouling challenges not fully captured in spiked models [40]. Second, the requirement for acidic dissolution of quantum dots for the SWASV readout necessitates a discontinuous, multi-step workflow, which currently precludes the single-step, real-time kinetic monitoring achievable by reagent-free electrochemical sensing architectures. Future work will focus on addressing these translational gaps, adapting this platform for the multiplexed detection of a panel of exosomal biomarkers, and integrating the sensor into a portable, automated device to facilitate its use in point-of-care diagnostics.

Authors' Contributions

W.Y. and S.J. carried out the experiments, data acquisition, and data analysis. C.M., J.J., and K.Z. contributed to methodology development and validation. D.L. provided resources, technical support, and clinical sample supervision. J.T. conceived the study, designed the research, and supervised the overall project. All authors contributed to the writing, critical revision, and final approval of the manuscript.

Availability of Data and Materials

All data generated or analyzed in this study are included in this published article and its supplementary information files. Additional raw data are available from the corresponding author upon reasonable request.

Conflict of Interests

The authors declare that they have no known competing financial interests or personal relationships that could have appeared to influence the work reported in this manuscript.

References

[1] Castellanos-Rizaldos, E., Grimm, D. G., Tadigotla, V., Hurley, J., Healy, J., Neal, P. L., Sher, M., Venkatesan, R., Karlovich, C., Raponi, M. et al. Exosome-based detection of EGFR T790M in plasma from non–small cell lung cancer patients. *Clin Cancer Res* **24**, 2944–2950 (2018).

[2] Carreca, A. P., Tinnirello, R., Miceli, V., Galvano, A., Gristina, V., Incorvaia, L., Pampalone, M., Taverna, S. and Iannolo, G. Extracellular vesicles in lung cancer: implementation in diagnosis and therapeutic perspectives. *Cancers* **16**, 1967 (2024).

[3] Zhou, T., Ma, H., Li, Z., Xu, Y. and Zhao, L. Exosomes in lung cancer: a role in early diagnosis. *Front Oncol* **15**, 1599608 (2025).

[4] Li, X., Corbett, A. L., Taatizadeh, E., Tasnim, N., Little, J. P., Garnis, C., Daugaard, M., Guns, E., Hoorfar, M. and Li, I. T. S. Challenges and opportunities in exosome research: perspectives from biology, engineering, and cancer therapy. *APL Bioeng* **3**, 011503 (2019).

[5] Imran, M., Shahzadi, I., Haider, A., Hassan, M., Ul-Hamid, A., Safdar, W., Haider, J. and Ikram, M. Catalytic and antibacterial activities with molecular docking analysis of chitosan and polyethylene glycol–NiO_2 nanostructures. *J Nanostruct Chem* **15**, 152520 (2025).

[6] Xu, Y., Wan, L., Zare, N., Wang, S.-W. and Lei, Z. Cr_2C MXene modification of an electrochemical platform allows for highly selective and sensitive detection of PSMA, a prostate cancer biomarker. *J Nanostruct Chem* **15**, 152517 (2025).

[7] Stanciu, L. A., Wei, Q., Barui, A. K. and Mohammad, N. Recent advances in aptamer-based biosensors for global health applications. *Annu Rev Biomed Eng* **23**, 433–459 (2021).

[8] Mutlu, E., Kaya, Ö., Yildirim, A. B. and Çetinkaya, A. Exosome production, isolation and characterization from A549 epithelial carcinoma cells. *Hacet J Biol Chem* **47**, 383–388 (2020).

[9] Lobb, R. J., Becker, M., Wen Wen, S., Wong, C. S., Wiegmans, A. P., Leimgruber, A. and Möller, A. Optimized exosome isolation protocol for cell culture supernatant and human plasma. *J Extracell Vesicles* **4**, 27031 (2015).

[10] Chen, F., Mostafiz, B., Suni, J. and Peltola, E. Electrochemical design of gold nanostructures for controllable electrochemical performance and scalable aptamer sensing application. *ACS Appl Nano Mater* **8**, 9812–9823 (2025).

[11] Švorčík, V., Siegel, J., Šutta, P., Mistrík, J., Janíček, P., Worsch, P. and Kolská, Z. Annealing of gold nanostructures sputtered on glass substrate. *Appl Phys A* **102**, 605–610 (2011).

[12] Song, R., Liu, Y. and He, L. Synthesis and characterization of mercaptoacetic acid-modified ZnO nanoparticles. *Solid State Sci* **10**, 1563–1567 (2008).

[13] Hurling, S. Introduction to EDC. *New Dir Teach Learn Engl Discuss* **1**, 2–10 (2012).

[14] Liu, Y., Canoura, J., Alkhamis, O. and Xiao, Y. Immobilization strategies for enhancing sensitivity of electrochemical aptamer-based sensors. *ACS Appl Mater Interfaces* **13**, 9491–9499 (2021).

[15] Nooranian, S., Mohammadinejad, A., Mohajeri, T., Aleyaghoob, G. and Kazemi Oskuee, R. Biosensors based on aptamer-conjugated gold nanoparticles: a review. *Biotechnol Appl Biochem* **69**, 1517–1534 (2022).

[16] Wang, J., Liu, G., Polsky, R. and Merkoçi, A. Electrochemical stripping detection of DNA hybridization based on cadmium sulfide nanoparticle tags. *Electrochem Commun* **4**, 722–726 (2002).

[17] Fan, F., Dou, J., Ding, A., Zhang, K. and Wang, Y. Determination of lead by square wave anodic stripping voltammetry using an electrochemical sensor. *Anal Sci* **29**, 571–577 (2013).

[18] Malenica, M., Vukomanović, M., Kurtjak, M., Masciotti, V., Dal Zilio, S., Greco, S., Lazzarino, M., Krušić, V., Perčić, M., Jelovica Badovinac, I. et al. Perspectives of microscopy methods for morphology characterisation of extracellular vesicles from human biofluids. *Biomedicines* **9**, 603 (2021).

[19] Reclusa, P., Sirera, R., Araujo, A., Giallombardo, M., Valentino, A., Sorber, L., Bazo, I. G., Pauwels, P. and Rolfo, C. Exosomes genetic cargo in lung cancer: a truly Pandora's box. *Transl Lung Cancer Res* **5**, 483 (2016).

[20] Bielska, E., Harrison, P. et al. Minimal information for studies of extracellular vesicles 2018 (MISEV2018): a position statement of the International Society for Extracellular Vesicles and update of the MISEV2014 guidelines. *J Extracell Vesicles* **7**, 1535750 (2018).

[21] Giannopoulos-Dimitriou, A., Saiti, A., Malousi, A., Anagnostopoulos, A. K., Vatsellas, G., Al-Maghrabi, P. M., Müllertz, A., Fatouros, D. G. and Vizirianakis, I. S. Molecular profiling of A549 cell-derived exosomes: proteomic, miRNA, and interactome analysis for identifying potential key regulators in lung cancer. *Cancers* **16**, 4123 (2024).

[22] Sandua, A., Alegre, E. and Gonzalez, A. Exosomes in lung cancer: actors and heralds of tumor development. *Cancers* **13**, 4330 (2021).

[23] Liu, W., Howarth, M., Greytak, A. B., Zheng, Y., Nocera, D. G., Ting, A. Y. and Bawendi, M. G. Compact biocompatible quantum dots functionalized for cellular imaging. *J Am Chem Soc* **130**, 1274–1284 (2008).

[24] Ji, Y., Yang, X., Ji, Z., Zhu, L., Ma, N., Chen, D., Jia, X., Tang, J. and Cao, Y. DFT-calculated IR spectrum amide I, II, and III band contributions of N-methylacetamide fine components. *ACS Omega* **5**, 8572–8578 (2020).

[25] Badilescu, S., Raju, D., Bathini, S. and Packirisamy, M. Gold nano-island platforms for localized surface plasmon resonance sensing: a short review. *Molecules* **25**, 4661 (2020).

[26] Potejanasak, P. and Duangchan, S. Gold nanoisland agglomeration upon the substrate assisted chemical etching based on thermal annealing process. *Crystals* **10**, 533 (2020).

[27] Tesler, A. B., Maoz, B. M., Feldman, Y., Vaskevich, A. and Rubinstein, I. Solid-state thermal dewetting of just-percolated gold films evaporated on glass: development of the morphology and optical properties. *J Phys Chem C* **117**, 11337–11346 (2013).

[28] Lee, M. R., Lee, H. K., Yang, Y., Koh, C. S. L., Lay, C. L., Lee, Y. H., Phang, I. Y. and Ling, X. Y. Direct metal writing and precise positioning of gold nanoparticles within microfluidic channels for SERS sensing of gaseous analytes. *ACS Appl Mater Interfaces* **9**, 39584–39593 (2017).

[29] Kim, Y., Park, J., Choi, D., Jang, H., Lee, J., Park, H., Choi, J., Ju, D., Lee, J. and Kim, D. ITO/Au/ITO multilayer thin films for transparent conducting electrode applications. *Appl Surf Sci* **254**, 1524–1527 (2007).

[30] Yang, G. and Liu, G. New insights for self-assembled monolayers of organothiols on Au(111) revealed by scanning tunneling microscopy. *J Phys Chem B* **107**, 8746–8759 (2003).

[31] Oberhaus, F. V., Frense, D. and Beckmann, D. Immobilization techniques for aptamers on gold electrodes for the electrochemical detection of proteins: a review. *Biosensors* **10**, 45 (2020).

[32] Sahoo, S. R. and Ke, S.-C. Spin-orbit coupling effects in Au 4f core-level electronic structures in supported low-dimensional gold nanoparticles. *Nanomaterials* **11**, 554 (2021).

[33] Mirsaleh-Kohan, N., Bass, A. D. and Sanche, L. X-ray photoelectron spectroscopy analysis of gold surfaces after removal of thiolated DNA oligomers by ultraviolet/ozone treatment. *Langmuir* **26**, 6508–6514 (2010).

[34] Shon, Y.-S., Aquino, M., Pham, T. V., Rave, D., Ramirez, M., Lin, K., Vaccarello, P., Lopez, G., Gredig, T. and Kwon, C. Stability and morphology of gold nanoisland arrays generated from layer-by-layer assembled nanoparticle multilayer films: effects of heating temperature and particle size. *J Phys Chem C* **115**, 10597–10605 (2011).

[35] Ma, H., Li, J., Gao, M., Dong, Y., Luo, Y. and Su, S. An electrochemical aptasensor for accurate and sensitive detection of exosomes based on dual-probe recognition and hybridization chain reaction. *Biosensors* **15**, 302 (2025).

[36] Li, J., Liu, Y., Wang, C., Jia, Q., Zhang, G., Huang, X., Zhou, N. and Zhang, Z. Determination of VEGF165 using impedimetric aptasensor based on cyclohexanehexone-melem covalent-organic framework. *Microchim Acta* **188**, 211 (2021).

[37] Kayiş, E. Ç., Torul, H., Sazaklıoğlu, S. A., Çelikkan, H., Ensarioğlu, H. K., Gumus, B. H., Vatansever, H. S. and Tamer, U. Electrochemically generated paper SERS substrate for detection of exosome in urine samples. *Sens Actuators B Chem* **426**, 137103 (2025).

[38] Im, Y., Yoo, H., Ko, R.-E., Lee, J. Y., Park, J. and Jeon, K. Exosomal CD63 in critically ill patients with sepsis. *Sci Rep* **11**, 20300 (2021).

[39] Wang, C.-K., Tsai, T.-H. and Lee, C.-H. Regulation of exosomes as biologic medicines: regulatory challenges faced in exosome development and manufacturing processes. *Clin Transl Sci* **17**, e13904 (2024).

[40] Suthar, J., Prieto-Simon, B., Williams, G. R. and Guldin, S. Dual-mode and label-free detection of exosomes from plasma using an electrochemical quartz crystal microbalance with dissipation monitoring. *Anal Chem* **94**, 2465–2475 (2022).